PAPER

Organically modified clay with potassium copper hexacyanoferrate for enhanced Cs+ adsorption capacity and selective recovery by flotation†

Huagui Zhang, [ID] *[a] Yun Kon Kim,[b] Timothy N. Hunter,[a] Andrew P. Brown,[a] Jae W. Lee[b] and David Harbottle [ID] *[a]

The selective capture of mobile radioactive nuclides, such as $^{137}Cs^+$, is crucial to the clean-up and remediation of contaminated environments. While remediation remains a challenging task, the current study considers novel organo-clay composites containing potassium copper hexacyanoferrate (KCuHCF) as a viable option for large-scale clean-up. A three-step synthesis has been demonstrated whereby pristine montmorillonite clay was readily modified to incorporate KCuHCF nanoparticles for enhanced and selective Cs^+ removal from aqueous environments. Alkyldiamine (DT) was used as an organic modifier to intercalate the clay and provided chelating sites to anchor copper onto the clay matrix, from which KCuHCF nanoparticles were subsequently grown *in situ via* the coordination of hexacyanoferrate precursors with the immobilized copper ions. The organo-clay–HCF composite particles exhibited a superior Cs^+ adsorption capacity ($q_m = 206$ mg g^{-1}), twice that of the pristine clay. The enhanced performance also extended to high Cs^+ selectivity in seawater, with the organo-clay–HCF composites demonstrating Cs^+ selectivity values in excess of 10^5 mL g^{-1}, two orders of magnitude greater than the pristine clay. Organo modification of the clay particles reduced the particle wettability, thus facilitating the separation of Cs-loaded composite particles from aqueous environments by collector-less flotation. Batch flotation experiments showed recovery efficiencies of the Cs-loaded composite particles of up to 90%, which was in great contrast to the low recovery of less than 15% for the Cs-loaded pristine montmorillonite. The current study provides a new concept for the treatment of contaminated aqueous environments.

1. Introduction

Nuclear power is seen as a viable option to address the global energy challenge due to efficient and clean energy production. While the industry is heavily regulated, risks of nuclear incident, such as that witnessed at the Fukushima Daiichi nuclear plant, must be planned for, as they can result in substantial environmental liability.[1] The release of radioactive isotopes, in particular $^{134}Cs^+$ and $^{137}Cs^+$, can result in a significant biohazard with the long-lived radionuclides (half-life ∼ 30 years) accumulating in the environment, and total depletion of radioactivity requiring approximately 1000 years.[2] Additionally, a significant volume of contaminated effluent is produced from normal nuclear power operations (*e.g.* within fuel cooling plants) which must also be treated on an ongoing basis. Cs^+ is highly soluble in water and readily migrates with the potential to produce wide spread contamination of land and water systems.

Several remediation strategies have been deployed to recover Cs^+ from radioactive wastes including chemical precipitation, membrane extraction, reverse osmosis, solvent extraction and ion exchange.[3] Ion exchange by selective adsorbent is a proven route to separate Cs^+ from aqueous environments, forming a concentrated waste more suitable for disposal. Accordingly, a series of inorganic Cs^+ adsorbents have been developed, among which zeolites,[4] crystalline silicotitanate,[5,6] vanadosilicate[7] and chalcogenides,[2,8,9] have been studied in detail due to high Cs^+ selectivity and excellent removal efficiencies. Nevertheless, the complexity of synthesis and cost-inefficiency greatly limit application for large-scale nuclear waste clean-up and remediation. In contrast, natural clay minerals which have also been used as adsorbents for radionuclides (*e.g.* Cs^+, Sr^{2+}, Co^{2+})[10,11] and other hazardous contaminants are readily available, low cost, and therefore suitable for scale-up. In particular, montmorillonite, a member of the smectite clays composed of two tetrahedral silica sheets surrounding a central octahedral sheet of alumina in a 2-1 layered structure, has been extensively adopted as a very efficient Cs^+ adsorbent with an adsorption capacity in the range 57–104 mg g^{-1}.[10–13] This relatively high adsorption capacity

[a]School of Chemical and Process Engineering, University of Leeds, Leeds, LS2 9JT, UK. E-mail: d.harbottle@leeds.ac.uk; prehz@leeds.ac.uk

[b]Chemical and Biomolecular Engineering, Korean Advanced Institute of Science and Technology, Daejeon, Republic of Korea

results from favourable structural properties including high cation exchange capacity (CEC), large surface area, high swelling capacity, good chemical and mechanical stability.[10,14]

An alternative group of adsorbents that are cost-effective and show high adsorption capacity are Prussian blue analogues (PBAs), namely the hexacyanoferrates (HCFs) of transition metals, wherein potassium copper hexacyanoferrate (KCuHCF) provides higher Cs^+ selectivity compared to other metal hexacyanoferrates.[15] Hexacyanoferrate(II) is an agent of high Cs^+ affinity and selectivity, with the small hydrated ions such as Cs^+ able to permeate through the cubic structure, while the larger competing ions are blocked from accessing the sorption sites.[15–18] However, the fine particle size of this type of adsorbent makes it difficult to separate from aqueous environments, so it is generally incorporated within supporting materials for effective Cs^+ adsorption and removal.[15,19] The main supporting materials are either polymer composites or mesoporous silica, both of which show limited Cs^+ adsorption capacity. Even though both the smectite clay and HCF have demonstrated relatively high Cs^+ uptake ability, to the best of our knowledge, reports of nanocomposites immobilizing HCF onto clays remain surprisingly scarce.[20]

In the current study we report an original and facile synthesis route for organo-clay–KCuHCF composite adsorbents. Montmorillonite clay was organically intercalated with ethylhexadecyldimethyl-ammonium-bromide and decorated with alkyldiamine, followed by the *in situ* synthesis of KCuHCF. Cationic surfactant was firstly intercalated into the clay interlayer to immobilize the alkyldiamine, which acts as a metal chelator for a Cu^{2+}–diamine complex, serving as an anchoring point for KCuHCF growth. This type of incorporation, with organo-clay being the supporting matrix, retains the high Cs^+ adsorption capacity of the clay and KCuHCF, along with modifying the surface of the clay to be hydrophobic and enable easy recovery of the composite particles by flotation. In the absence of clays the nano-sized KCuHCF particles remain dispersed in suspension and unrecoverable, but the apparent growth in particle size through incorporation with clays, and the increased surface hydrophobicity provide realization for a new concept in Cs^+ removal from contaminated aqueous environments. The structure and chemistry of the composite adsorbents were characterized using a series of techniques including powder X-ray diffraction (XRD), Fourier transform infrared spectroscopy (FTIR), X-ray photoelectron spectroscopy, scanning electron microscopy (SEM) and transmission electron microscopy (TEM). Component loadings were quantified by thermogravimetric analysis (TGA). Cs^+ adsorption was studied by measuring the kinetics and adsorption capacity in environments of varying pH and multi-component ionic solutions. Finally, the flotation performance of the Cs-loaded composites was studied using a laboratory batch flotation cell, with recovery performance measured as a function of the DT concentration.

2. Experimental

2.1 Chemicals

Montmorillonite clay (abbreviated as Mont., a naturally occurring mineral) of ~200 mesh (<74 μm) was purchased from Alfa

Aesar. Ethylhexadecyldimethylammonium-bromide (EHDA-Br; abbreviated as EH) with M_w of 378.5 g mol^{-1} was purchased from Merck Millipore (purity > 98.0%). The metal ligand of alkyl-1,3-diaminopropane (Duomen-T; abbreviated as DT) with M_w of 350 g mol^{-1}, alkyl group (R) ranging from C_{12} to C_{18}, was supplied by Akzo Chemicals (batch no. 1197752). Chemical structures of the EH and DT are given in Fig. 1a. Potassium hexacyanoferrate(II) ($K_4[Fe(CN)]_6 \cdot 3H_2O$, ACS reagent, ≥99%), copper sulfate ($CuSO_4 \cdot 5H_2O$, Reagent Plus, ≥99%) and cesium chloride (CsCl, analytical grade) were purchased from Sigma-Aldrich and used as received.

The cation exchange capacity (CEC) of the montmorillonite clay was found to be 90 meq./100 g. The CEC was determined by the sorption of 0.01 M Cu(II)–triethylenetetramine complex $[Cu \cdot Trien]^{2+}$ following the procedure outlined by Honty *et al.*[21] The concentration of $[Cu \cdot Trien]^{2+}$ was measured at 577 nm by UV spectroscopy (UV-1800 SHIMADZU). The BET specific surface area of the montmorillonite clay was determined to be 29.85 m^2 g^{-1} by N_2 adsorption isotherm using a Micromeritics TriStar 3000. The chemical composition of the montmorillonite clay was measured by X-ray fluorescence (XRF) spectrometry to be 2.20 wt% Na_2O, 2.39 wt% MgO, 20.80 wt% Al_2O_3, 66.86 wt% SiO_2, 0.06 wt% P_2O_5, 0.40 wt% SO_3, 0.70 wt% K_2O, 1.66 wt% CaO, 0.16 wt% TiO_2, 0.05 wt% MnO, 4.57 wt% Fe_2O_3, 0.03 wt% CuO, 0.01 wt% ZnO, 0.06 wt% SrO and 0.05 wt% ZrO_2.

2.2 Synthesis

Preparation of organo-clays (Mont–EH–DT). The montmorillonite clay particles were dispersed *via* stirring in ultrapure Milli-Q water (resistivity of 18.2 MΩ cm) for 3 h at a solid-to-liquid ratio of 30 g L^{-1}, and left undisturbed for 12 h to separate out any quartz sand and heavy minerals. The remaining stable suspension (non-sedimented portion) was then decanted and the particle concentration was measured by drying and adjusting to 20 g L^{-1} before being stored as stock fractioned suspension.

To organically modify the clay particles and generate reacting sites for HCF growth, a cationic surfactant of alkylammonium salt (EHDA-Br) was first used to intercalate the clay particles. While the irreversible binding of the cationic surfactant to the clay interlayers has not been verified in the current study, this likely interaction was previously reported.[22] The intercalated EHDA-Br molecules provided sites to anchor the metal ligand alkyldiamine (DT) through hydrophobic interactions. Without the inclusion of EHDA-Br, DT molecules were unable to bind to the clay particles as evidenced by previous research.[23] Immobilization of DT onto clay particles promotes both the hydrophobic modification of the clay particles and generates binding sites for the chelation of transition metals *via* a metal–diamine coordination mechanism, see Fig. 1a. 0.5 mL of 10 mM EHDA-Br solution was added dropwise to 20 mL of stock fractioned suspension (EH/Mont. ratio: 0.0125 mmol g^{-1}) in a 50 mL polypropylene centrifuge tube before agitating at 150 rpm in an orbital shaker for 2 h. The suspension was then centrifuged at 11 000 rpm for 15 min to separate the particles from any excess surfactant in the supernatant and washed
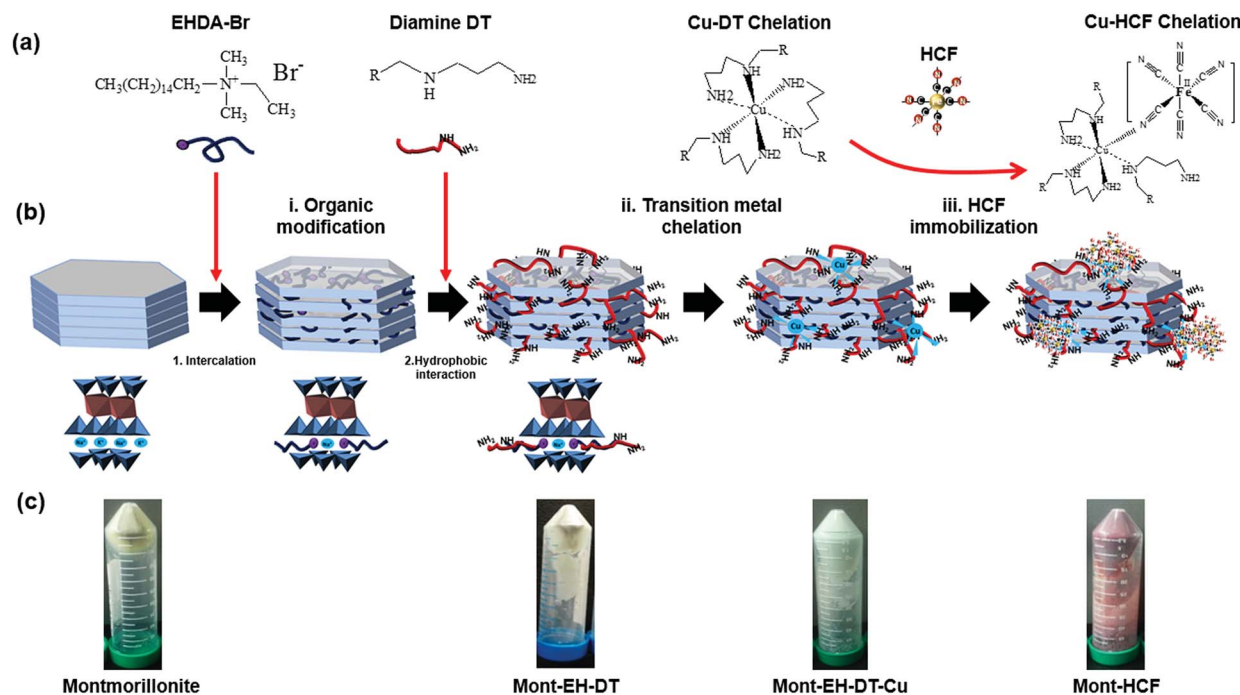
Fig. 1 (a) Structures of surfactant EHDA–Br, diamine DT, along with its chelation of copper, and the association with HCF. (b) Schematic representation of the three stage preparation procedure to form organo-clay–HCF composite adsorbent material: (i) organic modification including EH intercalation and hydrophobic interaction; (ii) chelation and (iii) immobilization. (c) Representative photos of wet samples at each stage of the preparation procedure. From left to right: montmorillonite, Mont–EH–DT, Mont–EH–DT–Cu and Mont–EH–DT–KCuHCF (*i.e.* Mont–HCF).

a further 3 times in Milli-Q water. The particles were then re-dispersed in a series of 20 mL DT solutions, with concentrations varying from 0.1 mM to 50 mM, details of which are specified in Table 1. The DT solutions were obtained by a series of dilutions from 0.5 M DT, and the solution pH was fixed between 8.5 and 9.0 to deprotonate both amine groups and minimize the possible displacement of pre-adsorbed EH, while ensuring that adsorption occurs through hydrophobic anchoring. The particle suspensions were shaken for 12 h before being rinsed in Milli-Q water a further 3 times, following the same procedure as outlined for removing excess DT.

Preparation of organo-clay–HCF composites (Mont–EH–DT–KCuHCF). To immobilize the hexacyanoferrate(II), the as-prepared organo-clay particles were re-dispersed in 10 mL

Milli-Q water before adding 10 mL 0.5 M $CuSO_4$ solution (solid content = 20 g L^{-1}). The suspension was shaken for 12 h to allow the metal receiving ligand anchored on the clay to chelate the Cu^{2+}. Then the as-obtained copper-chelated clays, of a light blue appearance (Fig. 1c), were washed in Milli-Q water for 3 times. Thereafter, the particles were dispersed in 20 mL 0.25 M $K_4Fe(CN)_6$ and shaken for 12 h following the same procedure as outlined for the Cu^{2+} anchoring process. The resulting Cu–DT complex is believed to have a slightly distorted octahedral geometry with one of the diamine ligands being labile such that it can be displaced by the cyano group from the ferrocyanide anion.[19] Once associated to the copper, an insoluble copper–ferrocyanide nanoparticle was formed, being immobilized onto the clay matrix *via* the associated DT chain anchoring. The

Table 1 Composition and theoretical adsorption capacity of Mont–HCF composite adsorbents

Sample label	Initial DT conc. (mM)	Organic loading[a] (% w/w)	Form of immobilized HCF[b]	HCF content[a] (% w/w)	q_m of organo-clay (mg_{Cs} g^{-1} organo-clay)[c]	Theoretical exchange capacity[d] (mg_{Cs} g^{-1} composite)
Pristine Mont.	0	0	—	0	103	103
Mont–HCF(DT0.1)	0.1	1.2	$K_{1.08}Cu_{1.46}Fe(CN)_6$	15.4	123	206
Mont–HCF(DT0.8)	0.8	1.8	$K_{1.76}Cu_{1.12}Fe(CN)_6$	16.0	97	188
Mont–HCF(DT8)	8	11.8	$K_{1.60}Cu_{1.24}Fe(CN)_6$	25.4	0	154
Mont–HCF(DT50)	50	40.4	$K_{1.66}Cu_{1.17}Fe(CN)_6$	35.8	0	225

[a] Estimated from the TGA data (Fig. S2). [b] Estimated from XPS analysis. [c] Obtained from Langmuir isotherm fitting of the experimental data, see Fig. S3. [d] Based on K^+ content in the immobilized HCF and the q_m of organo-clay matrix.

15132 | *J. Mater. Chem. A*, 2017, 5, 15130–15143

This journal is © The Royal Society of Chemistry 2017

resultant reddish brown product is denoted as Mont–EH–DT–KCuHCF with a shorter abbreviation of Mont–HCF. The modified clay particles were thoroughly washed with Milli-Q water to ensure that the particle suspension was free of dissolved salts. The modified clay particles were then divided into two groups; one fraction was oven dried at $T = 85$ °C and crushed into powder for characterization purposes, and a second fraction was re-dispersed in Milli-Q water to a solid concentration of 33.3 g L^{-1}, and kept wet for use in subsequent Cs$^+$ adsorption experiments.

2.3 Particle characterizations

Powder X-ray diffraction (XRD) patterns were obtained using a Bruker D8 X-ray diffractometer fitted with a LynxEye detector, using a Cu Kα (1.54 Å) radiation source operating at 40 kV and 40 mA, calibrated against a silica standard. Each sample was scanned over a 2θ angle range of 4° to 49.98° with a step size of 0.03299° at 2 s per step. Fourier transform infrared (FT-IR) spectra were collected using a Nicolet iS10 FT-IR spectrometer equipped with a deuterated triglycine sulphate (DTGS) KBr detector. A minimum of 36 scans were performed at a resolution 4 cm^{-1} in the range of 600 cm^{-1} to 4000 cm^{-1}. X-ray photoelectron spectroscopy (XPS) analysis was completed using a Thermo K-Alpha XPS system with a monochromated Al Kα X-ray source. An electron/ion gun was used to compensate for charge build-up on the sample during measurement. For morphological characterization, the as-prepared composite particles were deposited onto an SEM stub and dried in a desiccator before imaging using a Field Emission Gun Scanning Electron Microscope (FEG-SEM; LEO1530 GEMINI, Carl Zeiss Inc.). Transmission electron microscopy (TEM) measurements were completed using a FEI Tecnai TF20 FEG-TEM operated at 200 kV and fitted with a Gatan Orius SC600A CCD camera. Samples were prepared by depositing one drop of the particle suspension on an amorphous carbon film supported by a copper grid for TEM analysis (Agar Scientific Ltd). Elemental mapping of the modified clay particles in both the FEG-TEM and FEG-SEM was completed using energy dispersive X-ray spectroscopy (EDX) with an Oxford Instruments 80 mm^2 X-Max SD detector and INCA 350 software. Thermogravimetric analysis (TGA) was performed using ~20 mg samples in a Mettler-Toledo TGA-DSC1 instrument, with a heating profile from 30 °C to 1000 °C using a heating rate of 10 °C min^{-1} under steady N$_2$ flow (50 mL min^{-1}). The collected data were blank subtracted.

Contact angle. The three phase (particle–air–water) contact angle of the pristine and modified clay particles was evaluated by the sessile drop technique (Attension Theta tensiometer, KSV). The clay particles were compressed using a 2 ton load applied over an area of 13 mm^2 to form compressed disc substrates. A ~10 μL droplet of Milli-Q water was deposited on the surface of the compressed disc and the droplet contact angle was approximated using the Attension Software.

Particle size. Particle size was measured using a MasterSizer 2000 (Malvern Instruments Ltd., UK). Before each measurement the suspension was sonicated and then added drop-wise to the stirred measuring cell until the obscuration level was within a range of 5–10%. The size distribution of each particle sample was repeated 10 times with an average particle size reported.

Zeta potential. The particle zeta potential was measured using the acoustic zeta probe analyser (Colloidal Dynamics, USA). The suspension concentration was fixed at 0.16 w/w% and the suspension was stirred at 300 rpm. The measurements were performed under neutral condition in the pH range of 7–8.

2.4 Batch adsorption experiments

The composite particles were stored wet at a solid concentration of 33.3 g L^{-1}. Wet storage avoided any issues of particle clumping and mitigated the need for high energy re-dispersion in water. All batch adsorption experiments were completed using plastic vials to prevent Si contamination from glassware, and potential Cs$^+$ adsorption onto glassware, as previously discussed.[24] 19.4 mL cesium chloride (CsCl) solutions of varying electrolyte concentrations were prepared individually in polypropylene centrifuge tubes. 0.6 mL of the particle suspension was added to the electrolyte solutions and dispersed using mild sonication. The solid content was equal to 1 g L^{-1} (*i.e.* 20 mg solid in 20 mL liquid). The Cs$^+$ concentration was varied from 0.05 mM (6.6 ppm Cs$^+$) to 10 mM (1329 ppm Cs$^+$), with concentrations diluted from a stock solution of 100 mM CsCl. Particle suspensions were placed on an orbital shaker and shaken at 200 rpm for 48 h before centrifuging at 11 000 rpm for 15 min. The supernatant was decanted and passed through a 0.45 μm syringe filter before measuring the Cs$^+$ concentration in the supernatant by Atomic Adsorption Spectrophotometry (AAS, Varian 240FS spectrometer). Adsorption wavelengths of 852.1 nm and 455.5 nm were used to cover the range of sample concentrations. Before each measurement, calibrations were performed based on five standards properly diluted from a 1000 mg L^{-1} CsCl standard solution (Sigma-Aldrich).

The amount of cesium adsorbed by the particles, q (mg g^{-1}), was determined using the following equation:

$$q = \frac{(C_0 - C_e)V}{m} \tag{1}$$

where C_0 and C_e (both in units of ppm) are the initial and equilibrium Cs$^+$ concentrations, respectively (determined by AAS), V (L) is the volume of the suspension, and m (g) is the amount of adsorbent (clay or composite particles).

Adsorption kinetics were studied at a fixed initial Cs$^+$ concentration (C_0) of 1 mM, with the adsorption time varied from 10 min to 48 h. Adsorption experiments were conducted under neutral condition, except for the pH dependent study. The pH dependent Cs$^+$ adsorption by the organo-clay–HCF composites was evaluated across the pH range 2 to 12, with C_0 equal to 5 mM. The pH was adjusted using 1.0 M HCl and 1.0 M NaOH solutions for acidic and basic conditions, respectively. All other experimental procedures for adsorption testing remained consistent with those previously described (*i.e.* solid-to-liquid ratio = 1 g L^{-1}, shaking at 200 rpm for 48 h), with the equilibrium Cs$^+$ concentration in the supernatant measured by AAS. Cs$^+$ selectivity from other coexisting competitive ions was

This journal is © The Royal Society of Chemistry 2017

J. Mater. Chem. A, 2017, **5**, 15130–15143 | **15133**

considered by dispersing 0.02 g adsorbent particles (pristine montmorillonite and Mont–HCF(DT0.1)) in 20 mL seawater (untreated; Na$^+$: ~12 500 ppm, Mg^{2+}: ~1480 ppm, K$^+$: ~480 ppm, Ca^{2+}: ~150 ppm),[16] and dosing the seawater with 10 ppm Cs$^+$. After shaking for 48 h and following the separation procedure previously described, the final Cs$^+$ concentration in the supernatant was measured by inductively coupled plasma mass spectroscopy (ICP-MS, Perkin Elmer Elan DRCe).

2.5 Flotation experiments

Cs$^+$ contaminated (C_0 = 5 mM) composite particles were extensively washed with Milli-Q water (minimum of 3 washes) before being re-dispersed, and the solid concentration adjusted to 2 g L^{-1} (stored as stock suspension). In the current study the Cs$^+$ contaminated organo-clay–HCF particles were washed to remove excess electrolyte prior to flotation. While the washing step is not important in practice (*i.e.* following particle dispersion in the environment), the washing step was included to minimize the contribution from electrolyte-driven particle aggregation on the flotation performance. Flotation experiments were performed by pouring 100 mL stock suspension into the flotation cell, which is schematically shown in Fig. S1 of the ESI.† The flotation cell dimensions were 65 mm column diameter and 97 mm column height, with flotation bubbles generated at the base of the flotation column through a sintered glass plate. Milli-Q water was added to the particle suspension such that the total suspension volume equalled 210 mL (*i.e.* the initial solid concentration was fixed at 0.95 g L^{-1}). The air–suspension interface was ~5 mm below the froth collection outlet. Agitation of the particle suspension was provided by a 3/4 inch, 4-blade, 45° pitched impeller rotating at 300 rpm. During pre-treatment of the particle suspension the air flowrate was fixed at 1 sL per min. 20 μL methyl isobutyl carbinol (MIBC) was added as the frother (*i.e.* 80 ppm based on the total mass), and the particle suspension was mixed for 5 min. The impeller speed was then reduced to 100 rpm and the air flowrate increased to 8 sL per min to begin recovery of the organo-clays by flotation. (With no frother the launder foams were unstable, and recovery of the floated particles was compromised. In the environment addition of a frother may not be necessary due to the natural occurrence of organic species which will promote foam stabilization). The particle-laden foam was recovered *via* the side-arm of the flotation cell. Flotation experiments proceeded for 10 min and the foam was continuously collected. The collected foams were dried at 90 °C and weighed (m_d in g). The particle recovery (R%) was calculated using R% = m_d/m_0 × 100%, where m_0 is the initial particle mass in the suspension. Each flotation experiment was repeated a minimum of three times.

3. Results and discussion

3.1 Synthesis and characterization of organo-clay–HCF composite adsorbents

Organo-modification of the clays can be realized *via* intercalation of various cationic surfactants into the clay, albeit often to the detriment of the cation exchange capacity, which greatly limits the clays adsorption capacity for radionuclides.[14] In the current study, to simultaneously enhance the clay particle hydrophobicity as well as maintain or even improve the particles selective adsorption capacity of Cs$^+$, organo–montmorillonite composites containing potassium copper hexacyanoferrate (KCuHCF) nanoparticles were prepared, taking advantage of the copper–alkyldiamine coordination.

The particle synthesis route is a simple three-step process, which is schematically illustrated in Fig. 1b. (i) *Organic modification of the clay particles with the cationic surfactant (EH) and alkyldiamine (DT)*. EH surfactant molecules were intercalated into the montmorillonite (as confirmed by TGA analysis, shown in Fig. S2 of the ESI†), with the metal ligand DT anchored to the EH through hydrophobic interaction[23] to form an organo-clay of Mont–EH–DT. As is known, alkyldiamine chelates to a wide assortment of transition metal cations,[19] making the ligand a useful chelating agent to build different metal–ferrocyanides. Copper–ferrocyanide was chosen in the current study because of its high Cs$^+$ recovery.[15] (ii) *Copper chelation with the organo-clay particles*. The anchored DT acts as a chelator to immobilize copper, forming a Cu–DT complex, known for irreversibly associating with ferrocyanide anions.[19] (iii) *HCF immobilization*. The added hexacyanoferrate precursors coordinate with the copper ions at the amine (DT) sites, leading to efficient and selective *in situ* growth of KCuHCF nanoparticles. By varying the DT concentration, both the hydrophobicity and the HCF concentration on the modified clays can be well-controlled, delivering high Cs$^+$ adsorption capacity and good flotation performance. In the current study, the initial DT concentration was varied between 0.1 mM and 50 mM, including 0.8 mM and 8 mM, with the samples denoted as Mont–HCF(DT0.1), Mont–HCF(DT0.8), Mont–HCF(DT8) and Mont–HCF(DT50), respectively.

Powder X-ray diffraction (XRD) patterns of the Mont–HCF composites are shown in Fig. 2 and compared to pristine montmorillonite and KCuHCF as references. The pristine montmorillonite has a basal plane spacing (d_{001}) of 1.22 nm, which is in good agreement with previously reported data.[25] The *d*-spacing of the Mont–HCF composites expanded with increasing organic content to 1.27 nm and 1.34 nm for Mont–HCF(DT0.8) and Mont–HCF(DT8), respectively. The interlayer expansion suggests that the surfactant EH and ligand DT molecules are intercalated in the montmorillonite particles. The XRD patterns of the organo-clay–HCF composites, Mont–HCF(DT0.8) and Mont–HCF(DT8), have the characteristic diffraction peaks of montmorillonite, located at 2θ of 19.9° (111), 26.7° (103), 35.1° (211) (JCPDS card no. 60-0315), and additional peaks at 2θ values of 17.9°, 25.3° and 36.1°, which can be assigned to the (200), (220) and (400) planes of the cubic crystal structure of KCuHCF (with a cell constant of 9.99 Å; JCPDS card no. 02-0383). Thus, the XRD data confirms the presence of KCuHCF on the clay matrix. Moreover, the average crystallite size of the KCuHCF particles can be approximated using the Scherrer equation:

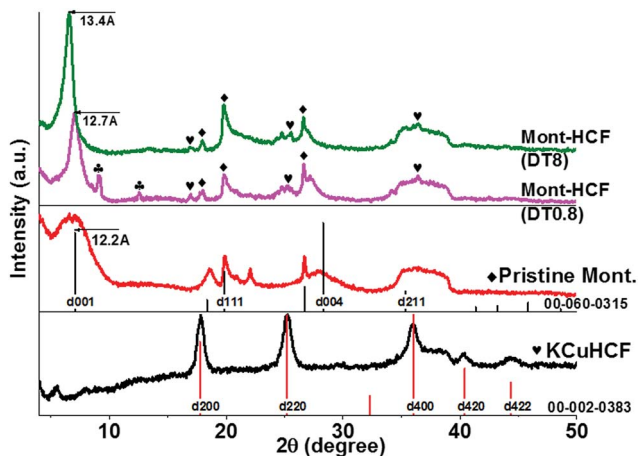$$L = \frac{K\lambda}{\beta \cos \theta} \qquad (2)$$

15134 | *J. Mater. Chem. A*, 2017, **5**, 15130–15143

This journal is © The Royal Society of Chemistry 2017

Fig. 2 XRD patterns of Mont–HCF composite adsorbents with DT loadings of 0.8 mM and 8 mM. Pristine Mont. (pattern file JCPDS-ICDD 00-060-0315), and bulk KCuHCF nanoparticle (pattern file JCPDS-ICDD 02-0383) shown as reference. ♣ symbol: peaks associated with clay textural changes.

where K is a dimensionless factor for crystal shape, taken to be 0.94,[18] λ is the X-ray wavelength (1.5406 Å for Cu Kα), θ is the diffraction angle at the peak (rad), and β is the full-width at half-maximum height (FWHM, rad). The average crystallite size for the KCuHCF complexes was determined from the major peaks (at 17.9°, 25.3° and 36.1°), and using eqn (2) the crystallite size was found to be 10.5 nm and 15.7 nm for Mont–HCF(DT0.8) and Mont–HCF(DT8), respectively. In the current study XRD was used to qualitatively assess the composition of the novel adsorbent, with quantitative assessment of the particle composition provided by TGA, see Fig. S2.† The characteristic peaks observed at ~9° and ~12° for Mont–HCF(DT0.8) result from partial textural changes in the clay structure, most likely associated with the dehydration of interlayer cations during sample drying. Such behavior is consistent with the characteristic diffraction patterns of heated (and oriented) montmorillonite samples reported in the ICDD database (*e.g.* JCPDS card no. 00-007-0304 and 00-060-0321), and more recently published data confirming a shift of the d_{001} plane from ~6° to ~9° following heat treatment.[26] These characteristic peaks were not observed for Mont–HCF(DT8) due to greater intercalation of organics, as evidenced by the reduction in the CEC (Table 1 and Fig. S3†). The relative intensities of the characteristic clay peaks were also affected by the change in clay texture, with stronger d_{001} and d_{111} peak intensities for the more exfoliated and therefore textured Mont–HCF(DT8) compared to Mont–HCF(DT0.8). Thus for Mont–HCF(DT0.8) the CuHCF peak intensities appeared more prominent.

FTIR spectra were collected for the initial reactants EH, DT and pristine montmorillonite; intermediate products of step (i) the organo-clay (Mont–EH–DT); and the final product of step (iii) the Mont–HCF composite, and are shown in Fig. 3a (from top to bottom). For montmorillonite (Mont.) the strong broad adsorption band with a peak at ~1000 cm^{-1} corresponds to the Si–O vibration of the tetrahedral silica sheet.[27] In the sample of organo-clay (Mont–EH–DT), the C–H stretching vibration peaks

between 2750 cm^{-1} and 3000 cm^{-1}, and the CH$_2$ bending vibration at 1470 cm^{-1} are assigned to the methylene moiety[15,23] of the surfactant EH and the ligand DT, consistent with the reference spectra of EH and DT. In addition, the band in the range of 1620–1640 cm^{-1} is characteristic of the –NH bending of the amine groups[10,15] originating here from DT, therefore confirming the successful preparation of organo-clays (Mont–EH–DT) in step (i). For the Mont–HCF composite (*i.e.* Mont–EH–DT–KCuHCF), when compared to the intermediate product Mont–EH–DT (step i), new peaks emerge at 2073 cm^{-1} and 2039 cm^{-1} and correspond to two closed CN stretching vibrations,[16,18,28] thus indicating the formation of the ferrocyanide (HCF) structure, and verifying the completion of steps (ii) and (iii). As previously reported, these two peaks have been attributed to the stretching of the CN ligand bridged between Cu^{2+} and Fe^{2+} in two different modes.[18] The success of step (ii) which features the copper–amine chelation is also demonstrated in the subsequent XPS analysis (Fig. 3b–f).

To further validate the success of the multi-step synthesis, XPS measurements on the intermediate product (step ii) of copper anchored organo-clay (Mont–EH–DT–Cu), and the final composite (step iii) of Mont–HCF were analysed using the sample Mont–HCF(DT0.8) as shown in Fig. 3b–f. Fig. 3b and d–f clearly show the presence of N 1s from DT/EH, and Cu 2p peaks in the sample of Mont–EH–DT–Cu. Although only weakly visible in Fig. 3b, these peaks are more pronounced in the high-resolution spectra shown in Fig. 3d and e. In particular, the peaks centred at 954 eV and 933 eV (Fig. 3e) were attributed to the Cu 2p$^{1/2}$ and Cu 2p$^{3/2}$ orbitals, respectively.[29] These peaks, together with the characteristic satellite peaks of Cu^{2+} at 962 eV and 943 eV, confirm the presence of copper ions in the intermediate and final composites. In addition, the XPS spectrum of Mont–HCF (Fig. 3b) identifies the peaks of Fe (2p) and K (2p), which results from the *in situ* growth of HCF (as confirmed from the reference spectrum of pure KCuHCF shown in Fig. 3b). From the C 1s deconvolution spectrum in Fig. 3c, two peaks centered at 283.92 eV and 285.69 eV were identifiable, which corresponded to the matrix C–C/C–H peaks and a C≡N group respectively.[28] In the N 1s spectra, the peak at 398.71 eV is characteristic of alkylammonium N, and the peak at 401.08 eV was assigned to the protonated amino group due to chelation with Cu^{2+} ions.[30] These peaks were observed in both the Mont–EH–DT–Cu and the Mont–HCF. When compared to the intermediate of step (ii) (Mont–EH–DT–Cu), a new strong peak at 397.11 eV was observed in the Mont–HCF, signifying the existence of N≡C ([Fe(CN)$_6$]$^{4-}$) in the composites. The XPS observations were consistent with the FTIR data shown in Fig. 3a. Moreover, the amino-copper chelation was confirmed from the Cu 2p$^{3/2}$ spectrum in Fig. 3f, where peaks centered around 932.0 eV were evident (*i.e.* 932.46 eV for Mont–EH–DT–Cu and 931.82 eV for Mont–HCF). This response, which is characteristic of Cu$^+$ species (~932 eV), appears as a result of the redox reaction of the chelated Cu^{2+} with the amino groups.[31] This peak becomes even more pronounced in the case of Mont–HCF when the ferrocyanide ([Fe(CN)$_6$]$^{4-}$) is immobilized with the C≡N coordinating to the copper–DT complex.
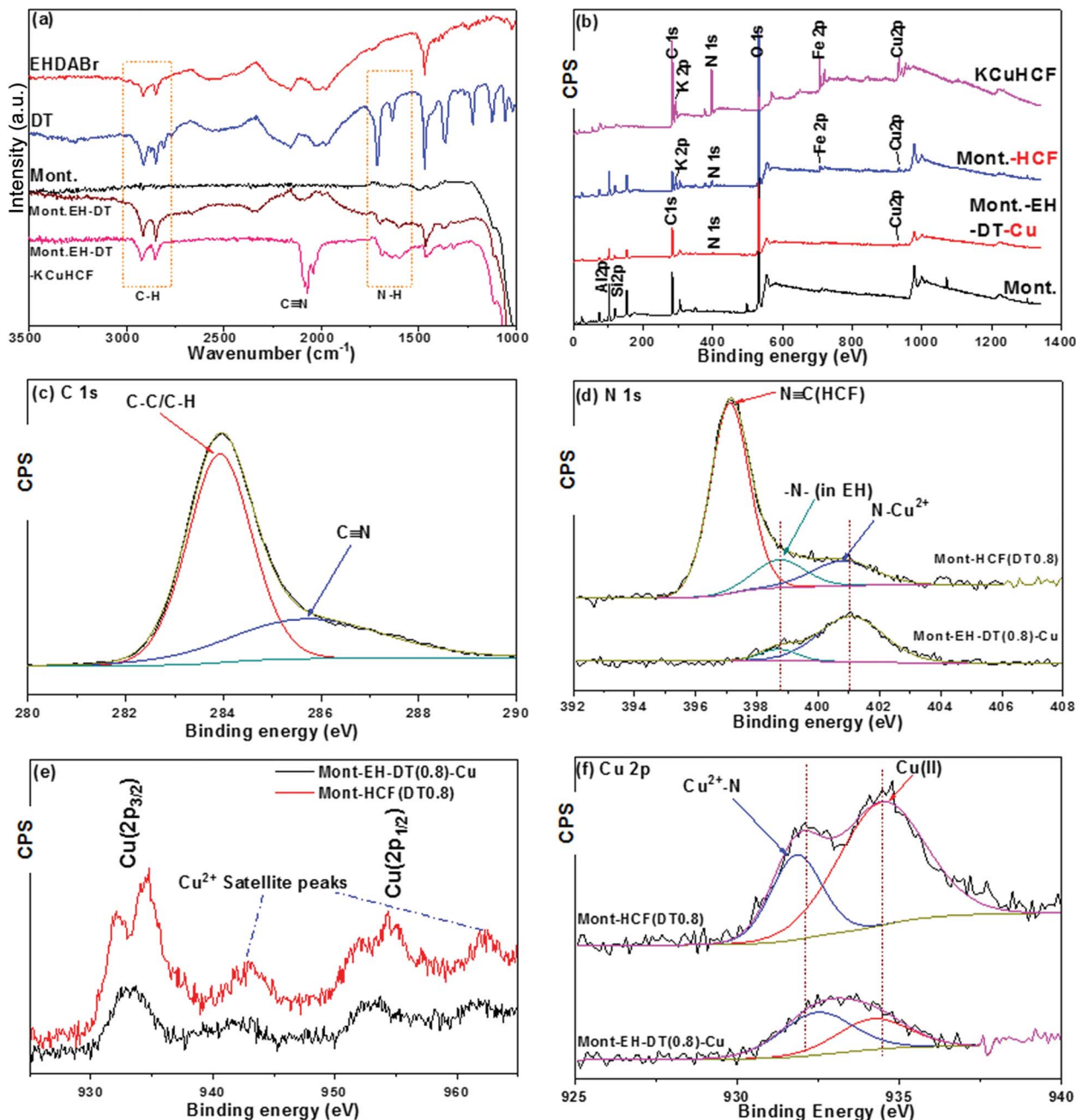
Fig. 3 (a) FTIR spectra of Mont−HCF composite and the intermediate product Mont−EH−DT of step (i), including the individual components Mont., EH, and DT as reference. (b) XPS survey spectra (full range) of Mont−HCF composite and the intermediate product Mont−EH−DT−Cu of step (ii), with Mont. and KCuHCF shown as reference. (c) High-resolution XPS spectrum on C 1s peak of Mont−HCF(DT0.8). (d−f) High-resolution XPS spectra on N 1s and Cu 2p peaks of Mont−EH−(DT0.8)−Cu and Mont−HCF(DT0.8).

From the FTIR and XPS analysis we can rationally conclude that Mont–HCF composites were successfully synthesized through the proposed copper–amine chelation mechanism. Depending on the amount of copper anchored by DT and subsequently reacted with an equivalent concentration of HCF precursor, the products of metal ferrocyanides prepared with different DT contents can be non-stoichiometric compounds. The relative atomic Cu/Fe ratios (Table S1 in ESI†) calculated from peak areas of the Cu 2p and Fe 2p peaks in the XPS spectra, were used to propose an 'equivalent' structure for the complex

according to the model structure $K_{2x}Cu_{(2-x)}[Fe(CN)_6]$.[32] Such an approach is reasonable since Fe was not found on the surface of pristine montmorillonite (Table S1†), and can be considered to be a specific element originating from HCF. The measured compositions of the copper ferrocyanide immobilized on to the montmorillonite surface are presented in Table 1.

Fig. 4 shows SEM images of pristine montmorillonite and the as-prepared Mont–HCF composites (DT0.8 and DT8), plus the N to Si atomic ratios of these compounds as determined by EDX spectroscopy. The "plate-like" structure of pristine
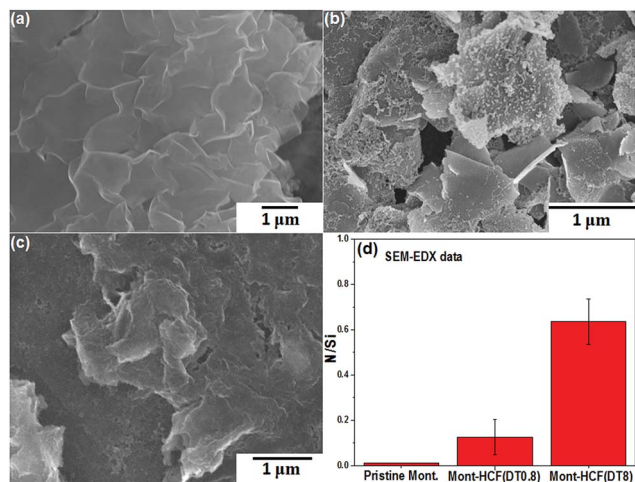
Fig. 4 SEM images of (a) pristine montmorillonite, (b) Mont–HCF(DT0.8), (c) Mont–HCF(DT8) composites, and (d) N/Si ratio determined from SEM-EDX analysis.

montmorillonite is clearly depicted in Fig. 4a. For Mont–HCF(DT0.8) (Fig. 4b), the silica basal plane becomes decorated with nano-sized particles, suggesting the presence of the KCuHCF nanoparticles on the montmorillonite surface. For Mont–HCF(DT8) (Fig. 4c), the inhomogeneous particle coverage appears to be replaced by a more uniform layer, forming a thin film and somewhat eliminating the sharp edge features of the pristine montmorillonite. The additional EDX data (Fig. 4d) shows that N, a characteristic element of DT and HCF, is detected in significant levels for both composite particles but not for the pristine montmorillonite. There is an incremental increase in N with nominal DT content (Fig. 4d). Both the SEM and EDX data further confirm the successful synthesis of organo-clay–KCuHCF composites.

The structure of the composite adsorbents was further characterized by TEM. Fig. 5a–f show TEM images of Mont–HCF(DT0.8) and Mont–HCF(DT8) particles, respectively. The Mont–HCF(DT0.8) clay particles retain a plate-like structure of nanosheets, with the surface partially covered by nanoparticles (Fig. 5a and b); the nanoparticles were identified to be KCuHCF by the crystal lattice spacings (Fig. 5b). Moreover, by imaging the lattice fringe at the clay edges (Fig. 5c), it was possible to estimate the clay interlayer spacing, which in the current study was measured to be 1.41 nm, consistent with the expansion due to intercalated organics; typical interlayer spacing for pristine montmorillonite was found to be ~1.0–1.2 nm.[14,25]

The TEM analysis is qualitatively consistent with the XRD data (Fig. 2). As the DT concentration on the clay particles increased, more Cu was anchored and hence more KCuHCF nanoparticles and/or larger KCuHCF particles were formed. This was confirmed by the crystalline structures on the Mont–HCF(DT8), see Fig. 5d and f. The Si, C, and N mass fractions on the particle surface were measured by XPS (Table S1†), and show a general trend of decreasing Si and increasing C and N with increased DT concentration, thus validating the progressive coating of the clay particle surface by HCF nanoparticles.

Fig. 5e shows a selected area electron diffraction (SAED) pattern taken from the highlighted region (red circle) in Fig. 5d. The SAED pattern for Mont–HCF(DT8) shows a strongly scattering clay lattice and weaker spots from the KCuHCF particles. Measurement of the latter leads to the labelled KCuHCF crystal, lattice planes (200) and (400) in Fig. 5e (JCPDS-ICDD no. 02-0383). In addition, lattice fringes of interplanar spacing of 0.246 nm were clearly visible in the high magnification TEM image (Fig. 5f), which corresponds to the (400) lattice plane of KCuHCF particles (JCPDS-ICDD no. 02-0383).

The organic content of the composite particles was determined by TGA, as shown in Fig. S2.† The pure organic components completely decomposed as the temperature increased from 200 to 400 °C. For pristine montmorillonite, a small but gradual weight loss is evident at ~700 °C, and this can be attributed to the dihydroxylation of the aluminium-silicate layer and the decomposition of any existing carbonate.[33,34] For pure KCuHCF, the first significant weight loss occurs in the range of 160 to 350 °C, which can be ascribed to both the elimination of coordinating water, this has been widely reported to exist in Prussian blue (PB)-like molecules (<250 °C),[15,28] and also the decomposition of the cyano group which has been shown to occur in the range of 250 to 350 °C.[15,35] At higher temperatures it is evident that the intermediate products undergo oxidative decomposition to iron oxides resulting in crystal growth, confirmed by the significant weight loss in the temperature range of 750–800 °C and the corresponding exothermic peak on the DSC curve (Fig. S2b†).[36,37]

For the organo-clays the thermal stability of the intercalated organics and the immobilized HCF was enhanced, as shown by the higher degradation temperatures across the temperature range 200 to 800 °C, with the two main weight losses observed around 400 °C and 600 °C. Considering the difference in mass loss between the intermediate organo-clay Mont–EH–DT and the final Mont–HCF composite product (Fig. S2c†), the mass fraction of KCuHCF nanoparticles in the composite particle can be estimated and is given in Table 1. Hence, a theoretical ion exchange capacity (TEC) can be calculated based on the potassium content of the immobilized HCF plus the maximum adsorption capacity (q_m) of the organo-clay matrix.

3.2 Batch adsorption experiments

Adsorption isotherm. To evaluate Cs$^+$ effluent removal performance by the organo-clay–HCF composites, batch adsorption experiments were performed and the adsorption isotherm, given in terms of mass adsorbate (Cs$^+$) to mass adsorbent, q in mg g^{-1}, was determined as a function of the equilibrium Cs$^+$ concentration (C_e in ppm) in solution. As a first approximation, the well-known Langmuir model which assumes surface monolayer sorption, finite number of binding sites, uniform sorption energies, as well as no transmigration of sorbates in the plane of the surface, was employed to describe the adsorption behavior. The Langmuir isotherm is given by:

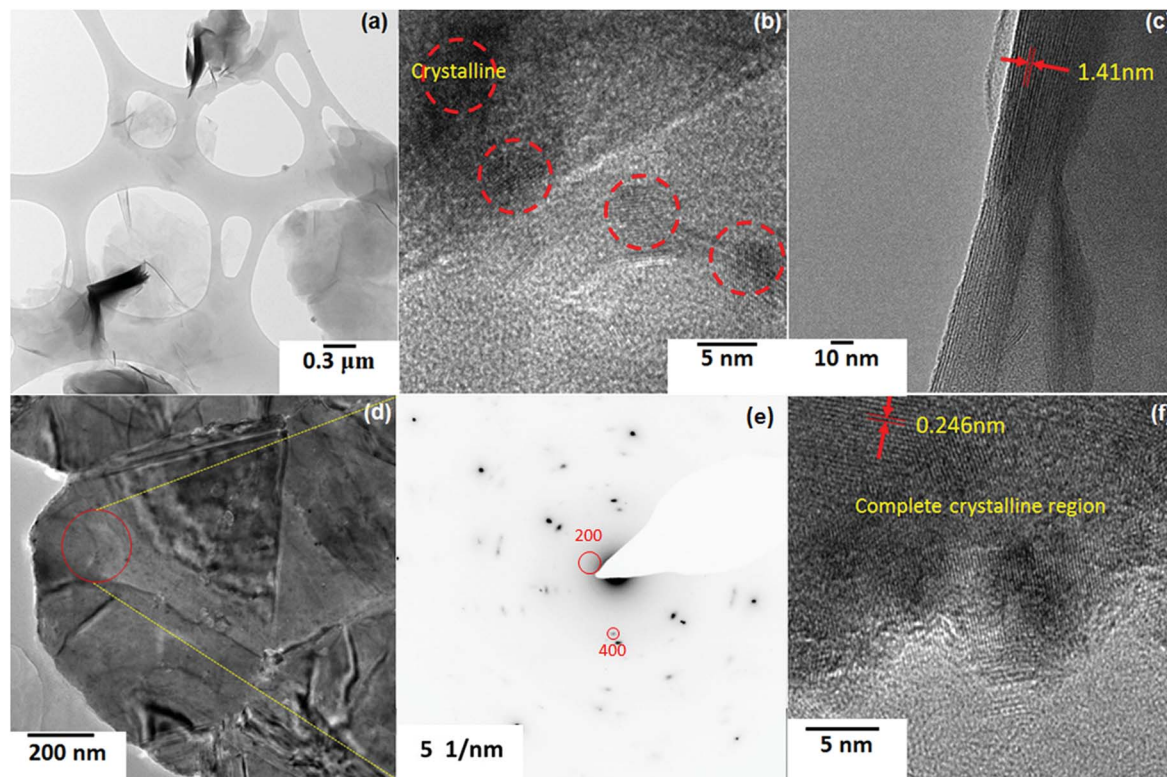$$q = \frac{bq_m C_e}{1 + bC_e} \tag{3}$$

Fig. 5 TEM images and electron diffraction pattern of composite adsorbents: (a–c) Mont–HCF(DT0.8); (d–f) Mont–HCF(DT8).

where b is the Langmuir constant related to the affinity coefficient of the binding sites (L mg^{-1}), and q_m is the maximum sorption capacity that describes the efficiency of Cs$^+$ removal from solution at or near saturation. As shown in Fig. 6a, the experimental data are in good agreement with the Langmuir isotherm. For each particle system the Langmuir fitting parameters q_m and b, and the correlation coefficients are listed in Table 2. Compared to the relatively low adsorption capacity of the pristine montmorillonite ($q_m \sim 103$ mg g^{-1}), the organo-clay–HCF composites demonstrated a significant enhancement in q_m, particularly Mont–HCF(DT0.1) with an adsorption capacity of 206.6 mg g^{-1}, twice that measured for the pristine montmorillonite. Such enhancement validates the successful immobilization of HCF onto the supporting montmorillonite particles given that both the clay particle and HCF can provide synergistic contributions for Cs$^+$ adsorption. Moreover, while the pristine montmorillonite particles reach an adsorption plateau at $C_e > 1000$ ppm, the adsorption of Cs$^+$ by the organo-clay–HCF composites plateaus at a much lower concentration ($C_e \sim 100$ ppm to 500 ppm), thus demonstrating the higher affinity to adsorb Cs$^+$. This behavior is consistent with the b values reported in Table 2.

It is worth noting that the apparent poor performance of the Mont–HCF composites with higher DT contents (*i.e.* DT8, DT50), as shown in Fig. 6b, resulted from a reduction in the adsorption capacity (CEC) of the clay matrix, brought about by the increased intercalation of DT. The reduced CEC with high DT concentration (*i.e.* DT8, DT50) was confirmed by measuring the Cs$^+$ adsorption capacity of the organo-clay intermediates

prior to HCF anchoring, which gave negligible values ($q_m \sim$ 0 mg g^{-1}) as shown in the ESI Fig. S3.† For the Mont–HCF composite adsorbents, a theoretical ion-exchange capacity (TEC) can be calculated based on the potassium content of the immobilized HCF and the experimentally measured q_m of the organo-clay matrix.

Since both parameters (HCF content, q_m of organo-clay matrix) vary for each composite, the TEC was calculated between 154 and 225 mg g^{-1} for increasing DT concentration (see Table 1). As shown in Fig. 6b, the TEC is in reasonable agreement with the experimentally determined maximum adsorption capacities (q_m). The fluctuating performance of the organo-clay–HCF composites (*i.e.* maximum q_m at DT = 0.1 mM and minimum q_m at DT 0.8 mM) can be attributed to the relative ion exchange capacities of both media (organo-clay and HCF content). At low DT concentrations (DT ≤ 0.8 mM) both the clay and bound HCF particles are active ion exchange sites, but with increasing DT concentration the organo-clay ion exchange capacity decreases (Table 1) and the HCF ion exchange capacity increases (directly related to the HCF content). Hence, the overall ion exchange capacity is a function of the relative contributions from both ion exchange sites. At higher DT concentrations the ion-exchange capacity of the organo-clay is effectively zero (Fig. S3†), hence q_m becomes a function of the HCF content only.

Such dependence has been validated by EDX mapping of the composite particles (see ESI Fig. S5†), where both the Cs and Fe peak intensities were higher for Mont–HCF(DT50) compared to Mont–HCF(DT8), confirming higher Cs$^+$ adsorption when the
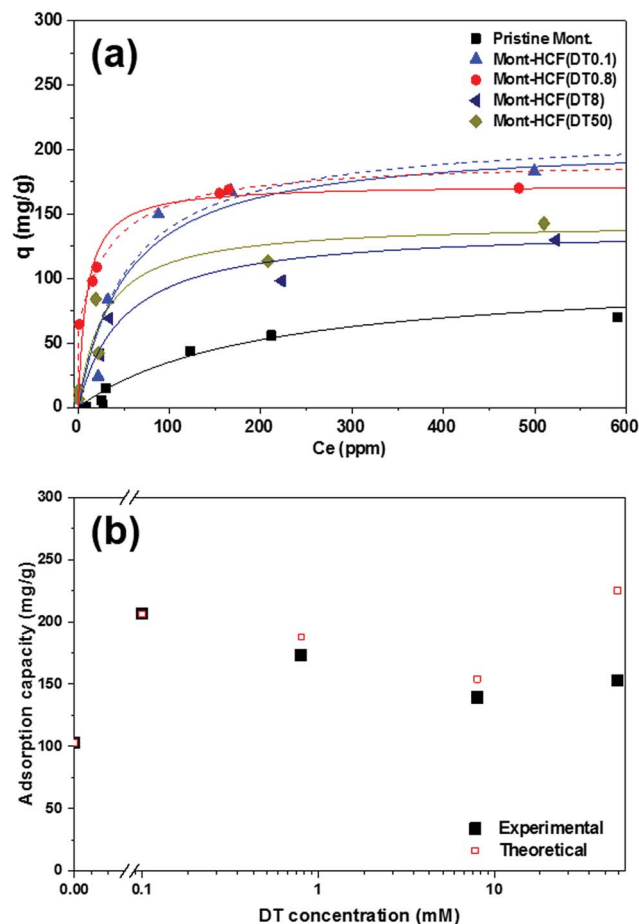
Fig. 6 (a) Cs$^+$ adsorption isotherm as a function of the equilibrium concentration (C_e) for Mont–HCF composites and pristine montmorillonite. Solid and dashed lines represent fittings by the Langmuir model (solid) and dual-site Langmuir model (dashed). (b) Comparison between the experimental and theoretical maximum adsorption capacities, q_m, for Mont–HCF composite particles as a function of DT concentration.

HCF concentration was higher. Likewise from XPS analysis, the higher Cs/Si ratio (Fig. S4†) for Mont–HCF(DT50) than Mont–HCF(DT8) and Mont–HCF(DT0.8) further supports this conclusion. Based on the TEC data we should observe a 25% increase in q_m between Mont–HCF(DT0.1) and Mont–HCF(DT50). While this enhancement demonstrates the added capacity through incorporation of more HCF, the practicality of

using Mont–HCF(DT50) particles is limited by the presence of many unbound HCF nanoparticles which results from HCF saturation of the clay matrix. Any unbound HCF particles remaining in the suspension (even though the particle suspension was washed several times), will result in an over-estimation of Cs$^+$ in the supernatant as measured by AAS (equivalent to an underestimation of Cs$^+$ adsorption), thus contributing to the deviation between theory and experiment for Mont–HCF(DT50) particles. Such difficulties associated with the removal of unbound HCF particles has been reported.[15]

In light of the fact that the Mont–HCF composites with DT0.1 and DT0.8 contain two possible active sites for ion sorption, the montmorillonite particle and the immobilized HCF, the dual-site Langmuir adsorption model was also considered, and describes sorption at two sites of different sorption energies. The dual-site Langmuir equation is given by:

$$q = \frac{b_1 q_{m1} C_e}{1 + b_1 C_e} + \frac{b_2 q_{m2} C_e}{1 + b_2 C_e} \qquad (4)$$

where the fitting parameters b_1, b_2 and q_{m1}, q_{m2} represent the affinity coefficients (L mg^{-1}) and the maximum sorption capacity (mg g^{-1}) for the two types of sorption sites, respectively. As shown in Fig. 6a, the dual-site Langmuir model (dashed line) describes the adsorption isotherm very well with the fitting parameters reported in Table 2. Such good agreement with distinct constants likely confirms that two binding sites, immobilized HCF and clay matrix, contribute to the adsorption of Cs$^+$.

XPS spectra of the organo-clay–HCF composite particles saturated with Cs$^+$ ($C_0 = 5$ mM) confirmed the significant displacement of K$^+$ by Cs$^+$, see Fig. S4.† Following Cs$^+$ adsorption the XRD data shown in Fig. 7 confirmed a reduction in the KCuHCF(200) peak height at 17.9° and a shift of the (220) and (400) planes to lower 2θ around 24.8° and 34.3°, confirming an effective crystal phase transition from KCuHCF to CsCuHCF (JCPDS card no. 24-0248). The XRD data suggest that the immobilized KCuHCF complex greatly contributes to Cs$^+$ adsorption *via* an ion-exchange mechanism, with these findings supported by the XPS data. In addition, a decrease in the clay (Mont–HCF(DT0.8)) *d*-spacing (d_{001}) from 1.27 nm to 1.22 nm implies that Cs$^+$ adsorption also occurred *via* isomorphic ion-substitution, leading to a slight reduction in the clay interlayer spacing, mainly due to the unfavourable hydration of the Cs$^+$ existing in the interlayer.[38]

Table 2 Cs$^+$ adsorption parameters obtained from Langmuir isotherm fittings

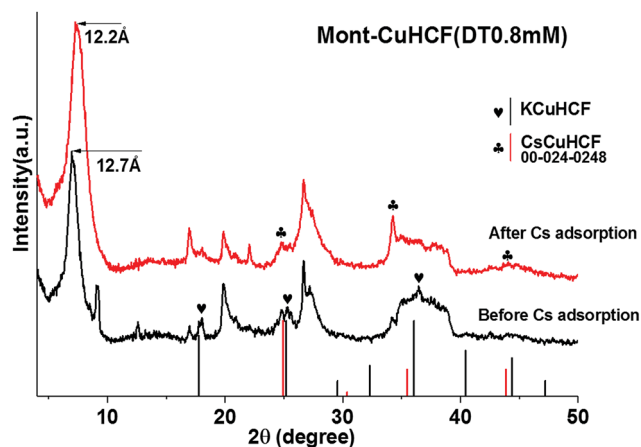| Sample	Langmuir			Dual-site Langmuir				
	q_m mg g^{-1}	b L mg^{-1}	R^2	q_{m1} mg g^{-1}	b_1 L mg^{-1}	q_{m2} mg g^{-1}	b_2 L mg^{-1}	R^2
Pristine Mont.	103.00	0.005	0.91					
Mont–HCF(DT0.1)	206.64	0.188	0.94	70.02	0.019	144.09	0.019	0.95
Mont–HCF(DT0.8)	173.05	0.109	0.91	60.79	0.003	131.68	0.027	0.98
Mont–HCF(DT8)	139.29	0.020	0.93					
Mont–HCF(DT50)	153.09	0.030	0.90					

Fig. 7 XRD patterns of Mont–HCF(DT0.8) before and after Cs⁺ adsorption (pattern file 00-024-0248 for CsCuHCF).

When compared to other clay-based adsorbents and KCuHCF adsorbents immobilized onto a range of different supporting materials, the Mont–HCF composites prepared in the current study are shown to be some of the most effective Cs⁺ adsorbents in terms of q_m. Adsorption capacity data from a number of studies has been compared to Mont–HCF(DT0.1) and are shown in Table 3.

Adsorption kinetics. Cs⁺ adsorption kinetics have been considered to compare the performance of Mont–HCF(DT0.8) to that of pristine montmorillonite (Fig. 8a). As shown, Cs⁺ adsorption by the pristine montmorillonite and the composite particle is reasonably fast, reaching equilibrium within a few hours. To quantitatively describe the adsorption kinetics the experimental data was fitted using a pseudo-second order rate equation (PSORE):

$$\frac{t}{Q_t} = \frac{1}{k_2 Q_e^2} + \frac{t}{Q_e} \tag{5}$$

where Q_t is the adsorbed Cs⁺ quantity (mg g⁻¹) at time t, Q_e is the adsorbed Cs⁺ quantity (mg g⁻¹) at equilibrium and k_2 is a rate constant. For both particles, Mont–HCF(DT0.8) and pristine montmorillonite, the PSORE fits are very good with an R^2 coefficient > 0.99, and the obtained fitting parameters reported in Table 4. Although the rate constant, k_2, for the composite adsorbent is lower than that for the pristine montmorillonite, the Cs⁺ uptake of the composite particle exceeds 80% within 30 min, compared to less than 5% for pristine montmorillonite under the same experimental conditions ($C_0 = 1$ mM). The $k_2 \times 10^2$ for the composite adsorbent equals 0.695 g mg⁻¹ min⁻¹ which is in good agreement with the previously published value of 0.65 g mg⁻¹ min⁻¹ for KCuHCF immobilized on chitin beads.[15]

pH effect. The stability and Cs⁺ adsorption performance of the composite adsorbent was investigated as a function of pH (Fig. 8b). In the pH range 4 to 12 ($C_0 = 5$ mM) the adsorption performance of the Mont–HCF(DT0.8) remained consistent, with the adsorption capacity, q_m, in the range of 169 to 176 mg g⁻¹. A small reduction in performance was observed in strongly acidic conditions (pH 2, $q_m = 155$ mg g⁻¹), which most likely resulted from the effect of competition between H⁺ and Cs⁺ ions. As reported elsewhere,[28] there is also a possibility that the Prussian-blue (PB) structure slightly denatures in strongly acidic conditions.

Competitive ion effect. The performance of the composite adsorbent was studied in more realistic aqueous environments, with the selectivity for Cs⁺ in complex cationic solutions (seawater) determined by dosing the seawater with 10 ppm Cs⁺. The distribution coefficient K_d is given by:

$$K_d = \frac{(C_0 - C_e)}{C_e} \frac{V}{m} \tag{6}$$

where C_0 and C_e are the initial and equilibrium concentrations of Cs⁺, V is the volume (mL) of the solution, and m is the mass (g) of the sorbent. Using eqn (6), pristine montmorillonite exhibited a relatively low Cs⁺ selectivity, $K_d = 1.81 \times 10^3$ mL g⁻¹,

Table 3 Cs⁺ adsorption capacities using modified montmorillonite particles, and metal hexacyanoferrate immobilized on different supports

Clay/Co-metal in HCF	Modifier/support	$q_m{}^a$ (mg$_{Cs}$ g⁻¹ composite)	Reference/publication year
Clay			
Montmorillonite	Pristine	57–104[b]	[10–12 and 38]/2013, 2011, 2002, 2009
Montmorillonite	Aluminum-pillared	83	[39]/2007
Montmorillonite	Phosphate	94	[11]/2011
Montmorillonite	Ethylamine	80	[10]/2013
Montmorillonite	Manganese oxide	90	[40]/2012
Montmorillonite	CuHCF(DT0.1)	206	Current study
Co-Metal in HCF			
Cu	Activated carbon	6	[41]/2009
Cu	Polyacrylonitrile (PAN)	26	[42]/2011
Cu	Chitin	118	[15]/2014
Cu	Mesoporous silica	177	[19]/2001
Cu	Montmorillonite(DT0.1)	206	Current study

^{a} Maximum adsorption capacity determined from Langmuir model. ^{b} The relatively wide range depends on the CEC of the specific type of montmorillonite.
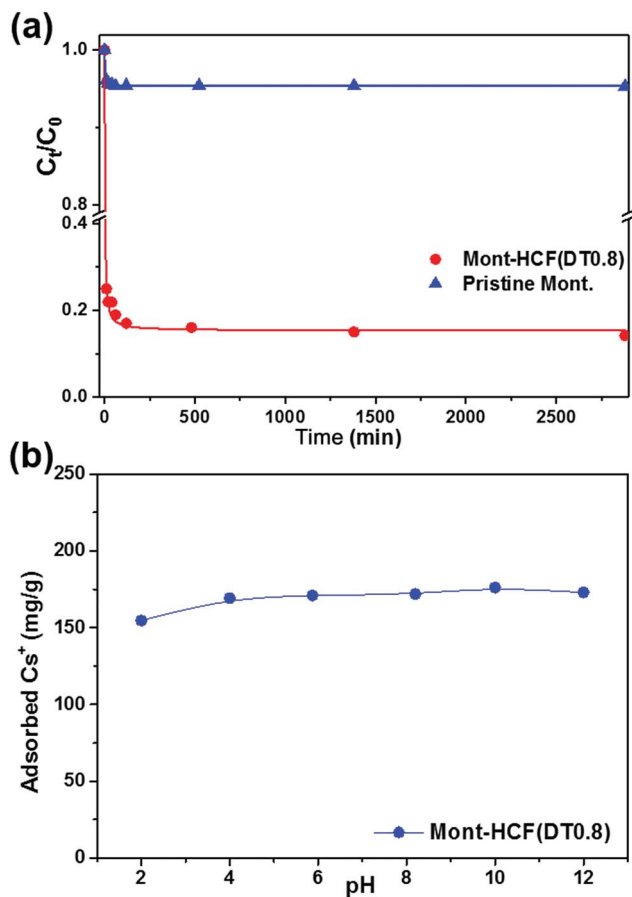
Fig. 8 (a) Cs$^+$ uptake kinetics for organo-clay–HCF composites, and pristine montmorillonite ($C_0 = 1$ mM). (b) Cs$^+$ adsorption as a function of the solution pH ($C_0 = 5$ mM).

Table 4 Kinetic parameters of Cs$^+$ adsorption determined by a fit of the pseudo-second order rate equation, eqn (5)

Sample	k_2 (g mg^{-1} min^{-1})	Q_e (mg g^{-1})	R^2
Pristine Mont.	0.09816	5.31	0.99
Mont–HCF(DT0.8)	0.00695	92.72	0.99

whereas Mont–HCF(DT0.1) resulted in a very high Cs$^+$ selectivity, $K_d = 1.10 \times 10^5$ mL g^{-1}. Such data confirmed that even in complex ionic environments composed of many competing cations, the composite adsorbent performs well in regards to Cs$^+$ adsorption, unlike pristine montmorillonite, which has previously been reported to perform poorly in competing cationic environments.[36,41] The significant enhancement in K_d for Mont–HCF(DT0.1) compared to pristine montmorillonite relates to the high Cs$^+$ selectivity of the HCF cubic structure. The cubic lattice of HCF acts as an ion sieve and preferential ion exchange with the lattice ions (i.e. pre-existing K$^+$) is governed by the size of the hydrated ion (Mg^{2+} (0.428 nm) > Na$^+$ (0.358 nm) > K$^+$ (0.331 nm) > Cs$^+$ (0.329 nm)).[43] The smaller hydrated ions such as Cs$^+$ can easily permeate into the lattice whereas larger hydrated ions such as Na$^+$ become size-excluded from the sorption sites.[28] Hence, HCF has high selectivity for Cs$^+$.

Moreover, the effect of DT content on the Cs$^+$ selectivity has been examined and was shown to be insignificant (data not shown), with K_d values within 2% over the DT concentration range studied.

3.3 Flotation selectivity

One of the objectives of this study was to synthesize organo-clays that exhibit high Cs$^+$ removal performance and can be easily recovered from the aqueous environment by flotation. Flotation performance of the Cs-loaded particles was studied using a laboratory flotation cell, as shown in Fig. S1 of the ESI.† The particle (mass) recovery percentage (R%) and the particle contact angle are shown in Fig. 9.

The flotation experiments were completed in the absence of any collector, i.e. collector-less flotation. As shown in Fig. 9, the recovery performance of the Cs-loaded montmorillonite was very poor, less than 15%, in comparison to the Cs-loaded Mont–HCF composite (Mont–HCF(0.1)), which has a recovery efficiency in the range of 80–90%. This significant difference can be attributed to an increase in the particle hydrophobicity induced via the interlayer intercalation and surface decoration of the clay particles by the organic components of EH and DT. This is also consistent with the measured contact angle data (Fig. 9) and the slight reduction in the particle zeta potential when the DT content increases (Table 5). These modifications to the
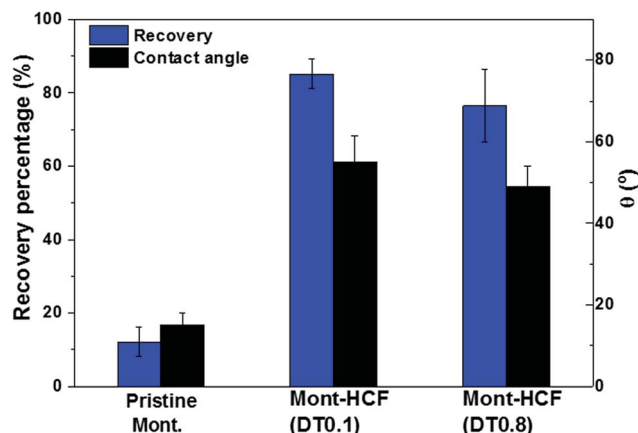

Fig. 9 Flotation recovery percentages of Cs-loaded particles ($C_0 = 5$ mM). The associated particle contact angles approximated by the sessile drop technique are shown on the second y-axis.

Table 5 Zeta potential and particle size of the composite and pristine montmorillonite particles

Adsorbents	Zeta potential^a (mV)	Particle size (μm)
Montmorillonite	−34.8 ± 3.1	3.3
Mont–HCF(DT0.1)	−24.7 ± 8.9	2.9/22.9^b
Mont–HCF(DT0.8)	−24.6 ± 1.9	2.9/13.2^b

^{a} Measurements were performed using Cs-loaded particles ($C_0 = 5$ mM).
^{b} Refers to the bimodal particle distribution.

particle surface properties promote slight aggregation of the composite particles and a broadening of the particle size distribution which may also contribute to the enhanced flotation performance, see Fig. S6 in the ESI.†

Together with the q_m data presented in Fig. 6, it is reasonable to conclude that the as-prepared Mont–HCF based composite particles demonstrate both high Cs^+ uptake and selectivity, along with excellent recovery by collector-less flotation. This approach provides a cost-effective route to treat large volumes of aqueous wastes, reducing the environmental contamination, and minimizing the volume of waste for further treatment and ultimate disposal.

4. Conclusions

A low cost and facile synthesis route has been demonstrated for organo-clay–HCF composites. The particle synthesis route included (i) organic modification of montmorillonite with cationic surfactant (EH) and alkyldiamine (DT), (ii) copper chelation with the anchored DT, and (iii) growth of $Cu^{2+}/[Fe(CN)_6]^{4-}/2K^+$ nanoparticles (KCuHCF) via the coordination between hexacyanoferrate precursors and the immobilized copper ions. XRD analysis confirmed the expansion of the clay interlayer due to adsorption of organics, along with identifying the crystal structure of KCuHCF nanoparticles. FTIR analysis confirmed the formation of CN bonds in the composite adsorbents implying the successful immobilization of HCF on the clay, which was further supported by EDX and XPS analysis. XPS also demonstrated that the KCuHCF immobilization was realized via a copper–amine coordination mechanism. SEM and TEM confirmed the decoration of the clay particles with sub 15 nm KCuHCF particles.

The DT concentration was varied between 0.1 mM and 50 mM, with increasing DT concentration resulting in the formation of more KCuHCF nanoparticles. However, at DT concentrations greater than 0.8 mM, a significant excess of KCuHCF nanoparticles were produced that were not well attached to the clay particles. These unbound particles were mostly unrecoverable following a series of sample washes, leading to apparent errors in the Cs^+ adsorption experiments when measured by Atomic Adsorption Spectrophotometry. Such production of unbound KCuHCF nanoparticles prohibited the use of Mont–HCF(DT8) and Mont–HCF–(DT50) composite adsorbents. For Mont–HCF(DT0.1) the Cs^+ adsorption capacity (q_m) was shown to be 206 mg g^{-1}, which was double the q_m for pristine montmorillonite particles. The excellent Cs^+ adsorption performance of the Mont–HCF composite was demonstrated over a wide pH range, as well as in seawater where the adsorption selectivity for Cs^+ in a complex solution of competing cations was shown to be superior compared to pristine montmorillonite, validating the robustness of the composite adsorbent.

The novel synthesis route not only enhanced the Cs^+ adsorption capacity of montmorillonite, but also increased the particle hydrophobicity. This effect allowed the Cs-loaded composite particles to be easily recovered by flotation, without the need for addition of flotation collectors. For the composite adsorbent,

recovery efficiency was in the range of 80 to 90%, compared to less than 15% for Cs-loaded pristine montmorillonite.

The current study has demonstrated a new concept for Cs^+ removal from aqueous environments. Rather than filtration through packed-bed columns, where blockages and chemical incompatibility can hinder performance, the novel approach to clean-up relies on the recovery of Cs-loaded clay particles by flotation, a technique that is suitable for remote deployment on any scale, facilitating the decontamination of environments, and minimizing the volume of waste for ultimate disposal.

Acknowledgements

Notes and references

1 D. H. Ding, Z. Y. Zhang, Z. F. Lei, Y. N. Yang and T. M. Cai, *Environ. Sci. Pollut. Res.*, 2016, **23**, 2249–2263.

2 J. L. Mertz, Z. H. Fard, C. D. Malliakas, M. J. Manos and M. G. Kanatzidis, *Chem. Mater.*, 2013, **25**, 2116–2127.

3 M. A. Olatunji, M. U. Khandaker, H. N. M. E. Mahmud and Y. M. Amin, *RSC Adv.*, 2015, **5**, 71658–71683.

4 S. Komarneni and R. Roy, *Science*, 1988, **239**, 1286–1288.

5 A. J. Celestian, J. D. Kubicki, J. Hanson, A. Clearfield and J. B. Parise, *J. Am. Chem. Soc.*, 2008, **130**, 11689–11694.

6 H. M. Liu, A. Yonezawa, K. Kumagai, M. Sano and T. Miyake, *J. Mater. Chem. A*, 2015, **3**, 1562–1568.

7 S. J. Datta, W. K. Moon, D. Y. Choi, I. C. Hwang and K. B. Yoon, *Angew. Chem., Int. Ed.*, 2014, **53**, 7203–7208.

8 N. Ding and M. G. Kanatzidis, *Nat. Chem.*, 2010, **2**, 187–191.

9 X. H. Qi, K. Z. Du, M. L. Feng, J. R. Li, C. F. Du, B. Zhang and X. Y. Huang, *J. Mater. Chem. A*, 2015, **3**, 5665–5673.

10 H. Long, P. X. Wu and N. W. Zhu, *Chem. Eng. J.*, 2013, **225**, 237–244.

11 B. Ma, S. Oh, W. S. Shin and S. J. Choi, *Desalination*, 2011, **276**, 336–346.

12 B. C. Bostick, M. A. Vairavamurthy, K. G. Karthikeyan and J. Chorover, *Environ. Sci. Technol.*, 2002, **36**, 2670–2676.

13 J. Q. Jiang and Z. Q. Zeng, *Chemosphere*, 2003, **53**, 53–62.

14 T. H. Wang, C. J. Hsieh, S. M. Lin, D. C. Wu, M. H. Li and S. P. Teng, *Environ. Sci. Technol.*, 2010, **44**, 5142–5147.

15 T. Vincent, C. Vincent, Y. Barre, Y. Guari, G. Le Saout and E. Guibal, *J. Mater. Chem. A*, 2014, **2**, 10007–10021.

16 Y. Kim, Y. K. Kim, S. Kim, D. Harbottle and J. W. Lee, *Chem. Eng. J.*, 2017, **313**, 1042–1050.

17 C. Loos-Neskovic, S. Ayrault, V. Badillo, B. Jimenez, E. Garnier, M. Fedoroff, D. J. Jones and B. Merinov, *J. Solid State Chem.*, 2004, **177**, 1817–1828.

15142 | *J. Mater. Chem. A*, 2017, **5**, 15130–15143

This journal is © The Royal Society of Chemistry 2017

18 R. Turgis, G. Arrachart, C. Delchet, C. Rey, Y. Barre, S. Pellet-Rostaing, Y. Guari, J. Larionova and A. Grandjean, *Chem. Mater.*, 2013, **25**, 4447–4453.

19 Y. H. Lin, G. E. Fryxell, H. Wu and M. Engelhard, *Environ. Sci. Technol.*, 2001, **35**, 3962–3966.

20 V. V. Strelko, V. K. Mardanenko, V. V. Yatsenko and N. Patrilyak, *Russ. J. Appl. Chem.*, 1998, **71**, 1746–1749.

21 M. Honty, M. De Craen, L. Wang, J. Madejova, A. Czimerova, M. Pentrak, I. Stricek and M. Van Geet, *Appl. Geochem.*, 2010, **25**, 825–840.

22 D. G. Devivo and B. L. Karger, *Sep. Sci.*, 1970, **5**, 145–167.

23 P. Malakul, K. R. Srinivasan and H. Y. Wang, *Ind. Eng. Chem. Res.*, 1998, **37**, 4296–4301.

24 J. Chorover, S. K. Choi, M. K. Amistadi, K. G. Karthikeyan, G. Crosson and K. T. Mueller, *Environ. Sci. Technol.*, 2003, **37**, 2200–2208.

25 C. W. Chiu and J. J. Lin, *Prog. Polym. Sci.*, 2012, **37**, 406–444.

26 M. S. Cavalcante, S. P. A. Paz, R. S. Angelica, E. N. Ito and R. F. Neves, *Clay Miner.*, 2016, **51**, 39–54.

27 J. Madejova, *Vib. Spectrosc.*, 2003, **31**, 1–10.

28 H. J. Yang, L. Sun, J. L. Zhai, H. Y. Li, Y. Zhao and H. W. Yu, *J. Mater. Chem. A*, 2014, **2**, 326–332.

29 Z. Y. Liu, Y. X. Hu, C. F. Liu and Z. Y. Zhou, *Chem. Commun.*, 2016, **52**, 12245–12248.

30 M. E. A. Ali, F. M. Hassan and X. S. Feng, *J. Mater. Chem. A*, 2016, **4**, 6620–6629.

31 L. Y. Chai, T. Wang, L. Y. Zhang, H. Y. Wang, W. C. Yang, S. Dai, Y. Meng and X. R. Li, *Carbon*, 2015, **81**, 748–757.

32 C. Loosneskovic, M. Fedoroff, E. Garnier and P. Gravereau, *Talanta*, 1984, **31**, 1133–1147.

33 L. Cabedo, D. Plackett, E. Gimenez and J. M. Lagaron, *J. Appl. Polym. Sci.*, 2009, **112**, 3669–3676.

34 D. Eliche-Quesada, C. Martinez-Garcia, M. L. Martinez-Cartas, M. T. Cotes-Palomino, L. Perez-Villarejo, N. Cruz-Perez and F. A. Corpas-Iglesias, *Appl. Clay Sci.*, 2011, **52**, 270–276.

35 J. H. Her, P. W. Stephens, C. M. Kareis, J. G. Moore, K. S. Min, J. W. Park, G. Bali, B. S. Kennon and J. S. Miller, *Inorg. Chem.*, 2010, **49**, 1524–1534.

36 Z. F. Jiang, D. L. Jiang, A. M. S. Hossain, K. Qian and J. M. Xie, *Phys. Chem. Chem. Phys.*, 2015, **17**, 2550–2559.

37 Q. F. Wu, G. L. Wu, L. D. Wang, W. L. Hu and H. J. Wu, *Mater. Sci. Semicond. Process.*, 2015, **30**, 476–481.

38 J. J. Wu, B. Li, J. L. Liao, Y. Feng, D. Zhang, J. Zhao, W. Wen, Y. Y. Yang and N. Liu, *J. Environ. Radioact.*, 2009, **100**, 914–920.

39 D. Karamanis and P. A. Assimakopoulos, *Water Res.*, 2007, **41**, 1897–1906.

40 Y. Park, W. S. Shin and S. J. Choi, *J. Radioanal. Nucl. Chem.*, 2012, **292**, 837–852.

41 L. Wang, M. Feng, C. X. Liu, Y. S. Zhao, S. Q. Li, H. Wang, L. Yan, G. Tian and S. J. Li, *Sep. Sci. Technol.*, 2009, **44**, 4023–4035.

42 A. Nilchi, R. Saberi, M. Moradi, H. Azizpour and R. Zarghami, *Chem. Eng. J.*, 2011, **172**, 572–580.

43 S. B. Yang, N. Okada and M. Nagatsu, *J. Hazard. Mater.*, 2016, **301**, 8–16.

This journal is © The Royal Society of Chemistry 2017

J. Mater. Chem. A, 2017, **5**, 15130–15143 | **15143**